InOOH-mediated Intergrown Heterojunctions for Enhanced Photocatalytic Performance: Assembly and Interfacial Charge Carrier Transferring

Farzin Nekouei[1], Xiaoming Wen[2], Zhong Zheng[3], Qingbo Sun[1], Teng Lu[1], Henry Orton[1], Felipe Kremer[4], Shahram Nekouei[5], Tongwei Yuan[1], Elwy H. Abdelkader[1], Borui Liu[6,7], Antonio Tricoli[7], Gottfried Otting[1], Zongwei Liu[3], Terry Frankcombe[8,*], Yun Liu[1,*]

[1]*Research School of Chemistry, The Australian National University, ACT 2601, Australia. E-mail: Yun.liu@anu.edu.au*
[2]*Center for Micro-Photonics, Swinburne University of Technology, VIC3122, Australia.*
[3]*School of Chemical and Biomolecular engineering, University of Sydney, NSW 2008, Australia.*
[4]*Centre for Advanced Microscopy, The Australian National University, ACT 2601, Australia.*
[5]*Young Researchers and Elites Club, Science and Research Branch, Islamic Azad University, Tehran, Iran.*
[6]*Nanotechnology Research Laboratory, Research School of Chemistry, College of Science, Australian National University, ACT 2601, Australia.*
[7]*Nanotechnology Research Laboratory, Faculty of Engineering, University of Sydney, NSW 2008, Australia.*
[8]*School of Science, The University of New South Wales, ACT 2601, Australia. email: t.frankcombe@adfa.edu.au*

Keywords: Intergrown heterojunction photocatalysts; $InOOH/In_2O_3$; $InOOH/ In(OH)_3$; interfacial charge transfer; perfluorooctanic acid

Abstract

Heterojunction photocatalysts with the appropriate band structure and abundant interfacial sites present promising photocatalytic performance. Research in this field has generally been focusing on incorporating dissimilar materials to prepare heterojunctions. Few studies show how to construct intergrown heterojunctions that structurally, the interfacial region is narrowed down to atomic scale, facilitating charge carrier transferring and avoiding potentially unfavoured band bending. This work for the first time reports the intergrowth of $InOOH/In(OH)_3$ and $InOOH/In_2O_3$ heterojunction photocatalysts and their greatly enhanced photocatalytic property towards perfluorooctanoic acid decomposition. The experimental and theoretical investigation indicate that band structure matching is essential for heterojunction photocatalysts. Fast interfacial charge carrier transferring offers additional charge carriers but does not always occur in the heterojunctions where other effects may play the dominated role in interfacial region. We believe that this comprehensive understanding of intergrown heterojunctions would benefit the design and application of high performance photocatalysts.

1. Introduction

Photoredox catalysis is a highly promising approach for many applications from solar-to-chemical energy conversion to waste water treatment [1-3]. Single-component semiconductive photocatalysts cover a broad solar spectral range but suffer from inefficient intrinsic charge

generation and recombination, resulting in a poor photocatalytic performance [4]. To overcome those weaknesses, heterostructured materials that integrate dissimilar materials with pristine interfaces are proposed for better control of charge transport and recombination [5, 6]. This strategy has been broadly employed. The rationally designed heterostructured materials have become essential, acting as a foundation of all modern electronics, optoelectronics, spintronics and photocatalysis [7]. Well-designed heterojunction photocatalysts have shown enhanced photocatalytic activity due to spatial separation of photogenerated electron–hole pairs [8]. The formation of Mott–Schottky junctions or semiconductor heterostructures (p-n junction or n–n/p-p junction with different materials) offer exciting possibilities to modulate the electron density distribution and thus promote charge separation and transfer [9]. It is evident that within hetero-structured photocatalysts, the interfaces play an essential role in band-binding, transforming, and transporting the surface species such as adsorbents, electrons, and subsequent reaction activity [10]. And therefore, the precise interface construction of hetero-structured photocatalysts with atomic scales is critical and may represent a promising strategy to maximize the photocatalysts performance, but the research with this regard has been rarely reported and less focussed.

Note that among the wide spectrum of semiconductors evaluated in recent decades, Indium-based family including indium oxide (In_2O_3), indium hydroxide ($In(OH)_3$), and indium oxyhydroxide (InOOH) have been extensively studied for a wide range of applications as sensors, electronics and photocatalysts [11, 12]. Particularly, compared to $In(OH)_3$ and InOOH, In_2O_3 has a narrower bandgap (~2.8-3.0 eV), high optical transparency, excellent stability, nontoxicity, proper band structure with suitable energy levels of the valence band (VB) and conduction band (CB), and a wider range absorption of solar radiation. This makes it suitable as a photocatalyst using both UV and Visible light for redox reactions. However, In_2O_3, like most other semiconductors, suffers from fast electron-hole recombination and slow

photoinduced electrons migration. Solving this issue requires more effort to be undertaken. For this purpose, various techniques have been recently studied, such as synthesizing different structures and morphologies using various precursors and experimental conditions [13, 14], doping with other elements [15, 16], creating more defect sites and oxygen vacancies [17, 18], and others. Furthermore, InOOH, as a typical indium-based wide band gap (~3.7 eV) and p-block metal oxyhydroxide, has become an attractive candidate for the removal of organic pollutants [19, 20]. Typically, it can serve as a precursor or intermediate to get In_2O_3. InOOH shows high redox capacity due to a notably low valance band energy level (~+3.38 eV, lower than In_2O_3). All these imply that the incorporation of p-block metal oxyhydroxide into a simple, narrow bandgap oxide might potentially be a strategy to design new photoelectrodes or photocatalysts [21]. Note that the incorporation of a small amount of rutile phase into an anatase phase, as two TiO_2 polymorphs, has been reported to improve the photocatalytic properties of anatase by the creation of a biphasic heterojunctions [22, 23]. Inspired by the above discussions, we demonstrate that incorporating *intergrown* assembly of heterojunctions between $In(OH)_3$ and In_2O_3 with InOOH (as an intermediate phase) can make resultant photocatalysts with greatly enhanced photocatalytic activity. Although there are a large number of studies on heterojunctions as photocatalysts by incorporating dissimilar materials [24, 25], there has been less attention on how the interfacial region is formed and how the charge carriers behaviour in this region accordingly. To the best of our knowledge, the formation of intergrown heterojunctions have not been reported and well-studied yet. To evaluate the photocatalytic performance of the studied materials in this work, perfluorooctanic acid (PFOA), as a recalcitrant and nonbiodegradable environmental polluting compound, was selected as a target. PFOA has been detected in indoor dust, soil, wildlife, water, foods, and human blood serum [26, 27], generating serious environmental and health issues. Thus, the need for effective and green technologies for PFOA removal are urgently being sought. As can be seen in **Figure S1**,

based on ISI Web of science data base, from 1990 to 2020, the number of papers published with title keywords of "*PFOA*", "*PFOS*" (for perfluorooctanoic acid and perfluorooctanesulfonic acid, respectively), and "*Environmental*" has remarkably increased illustrating the urgent need and interest for reliable methods for removal of fluorinated compounds.

2. Experimental section

2.1. Materials fabrication

$In(NO_3)_3 \cdot xH_2O$ (Aldrich), oleic acid (Aldrich) and urea (M&B) were used as raw materials to prepare photocatalysts. $In(OH)_3$ was first synthesized by a hydrothermal method using the following procedure: 1.5 g urea, 1 ml oleic acid and 35 mL deionized H_2O were mixed, preheated, and sonicated at 60°C for 30 min. Subsequently, 0.3 g of $In(NO_3)_3.xH_2O$ was added to the mixture and sonicated for another 30 min. The mixed solution was transferred and sealed into a 100 mL Teflon-lined autoclave and treated at 100 °C for 12 h. Finally, the product was collected and washed several times with deionized water and absolute ethanol and dried at 60 °C in air for 8 h. Other photocatalysts were obtained by heat-treating as-synthesized $In(OH)_3$ (PC0) under a controlled temperature for 3 h at 225°C, 325°C, 425°C, and 525°C and denoted as PC1-4, respectively. PC0 also be treated at 325°C for 1-4 hours. Commercialised $In(OH)_3$ nanopowder (Nanostructured and Amorphous Materials Inc.) was used and pure InOOH was also synthesized in this work for comparison.

2.2. Chemical and structural characterization

The crystal structure and phase of synthesized samples were determined by X-ray diffraction (XRD) technique using a powder diffractometer (Panalytical, $\lambda = 1.5406$Å). Scanning electron microscopy (Zeiss UltraPlus) and transmission electron microscopy (JEOL 2100F and aberration-corrected Themis Z scanning transmission electron microscope (S/TEM), FEI) were

used to observe their morphology, analyse chemical element and determine the nature of intergrown materials via atomic imaging. Differential scanning calorimetry (Thermo Analysis Q20) was used to determine the intergrown condition from synthesised $In(OH)_3$, and run in air from room temperature to 550°C. Nitrogen adsorption-desorption isotherm surface area measurements were carried out with a Tristar II BET instrument (Micromeritics).

2.3. Various spectral characterization

The optical absorption of materials was characterised by the PerkinElmer Lambda-465 UV−Vis spectrometer. X-ray photoelectron spectroscopy (XPS, Thermo Scientific: ESCALAB 250xi) was used for chemical and oxidation state analysis in which the bind energy was corrected using the referencing C 1s (284.8 eV). ^{1}H Nuclear magnetic resonance (NMR) spectrum was acquired at 700 MHz with a spinning rate of 40 kHz at room temperature and using a Phoenix NMR triple resonance broadband probe. Photoluminescent (PL) were collected to understand possible transferring behaviour of charge carriers, where the setup of steady PL allows the PL intensity quantitatively comparable and the time-resolved PL (TRPL) was performed with a time-correlated single photon counting system (PicoHarp 300, PicoQuant GmbH) and under the excitation of a 405 nm, 200 mW/cm^2 laser (pulse duration 40 ps, repetition rate 5 MHz).

2.4. Photocatalytic decomposition of PFOAs

To investigate the photocatalytic degradation of PFOAs, a 300mL PFOA water solution (20ppm) was mixed with a 100 mg photocatalyst in a quartz cylinder-shaped reactor. A chilli water cooled and quartz jacket protected UV lamp (254 nm, 100 W) was immersed into such a reactor for photocatalytic reaction as illustrated in **Figure S2**. Before light irradiation, the above mixture solution was sufficiently stirred to reach adsorption saturation to remove the effect of adsorption process. During the reaction period, the suspension solution (~1 mL) samples were

regularly collected, diluted and centrifuged to prepare the samples for ultra-high-performance liquid chromatography-MS/MS (UHPLC/MS/MS) characterisation. In this work, the PFOA concentration was detected by UHPLC/MS/MS instrument and its standard curve is presented in **Figure S3**. Detailed experimental information and acquired methods and set-up condition are given in **Table S1**.

3. Results and Discussion

3.1. Formation of intergrown heterojunctions

To determine heat treatment temperature of as-synthesised $In(OH)_3$, i.e. PC0, its differential scanning calorimetry (DSC) curve (solid curve in **Figure 1a**) was first collected, and additionally the commercialised $In(OH)_3$ is also measured under the same condition as a reference. Interestingly, it is found that the commercialised $In(OH)_3$ shows only one sharp endothermal peak at ~260ºC that directly links to the decomposition of $In(OH)_3$ into In_2O_3 [28, 29]. However, PC0 shows a significantly different scenario and two endothermal peaks are observed at ~270ºC and ~390ºC, respectively. As-synthesized PC0 exhibits another endothermic peak correlating with phase transition of InOOH to In_2O_3 which is reasonably consistent with previous literature [30]. **Figure S4** shows the illustration of probable phase transformation of pristine $In(OH)_3$ to In_2O_3 based on DSC results. PC0 is hence decided to be heat treated at 225°C, 325°C, 425°C and 525°C, respectively for three hours. The resultant samples are named after PC1-4. **Figure 1b** presents the XRD patterns of PC0-4. PC0 has a pure cubic phase with space group symmetry of Im-3. The main phase of PC1 is similar to that of PC0, except for two small peaks (marked with *) at 2θ of ~25º and ~33º. These two additional peaks are attributed to orthorhombic indium oxyhydroxide, i.e. InOOH, with a space group symmetry of *Pnnm*. This indicates PC1 is composed of the minor InOOH and dominated $In(OH)_3$ at 225 °C. Further increasing heat treatment temperature up to 325ºC, i.e. at the temperature above the first endothermal peak observed in the DSC curve, it is found that in the

resultant sample PC2, two weak diffraction peaks, previously assigned to InOOH, still present, but the predominated phase has already become In_2O_3, suggesting $In(OH)_3$ are completely decomposed, leading to the formation of dominated In_2O_3 and minor InOOH. When the heat treatment temperature increases up to 425 ºC (PC3) and 525 ºC (PC4), i.e. both above second endothermal peak presented in **Figure 1a**, only In_2O_3 phase is observable.

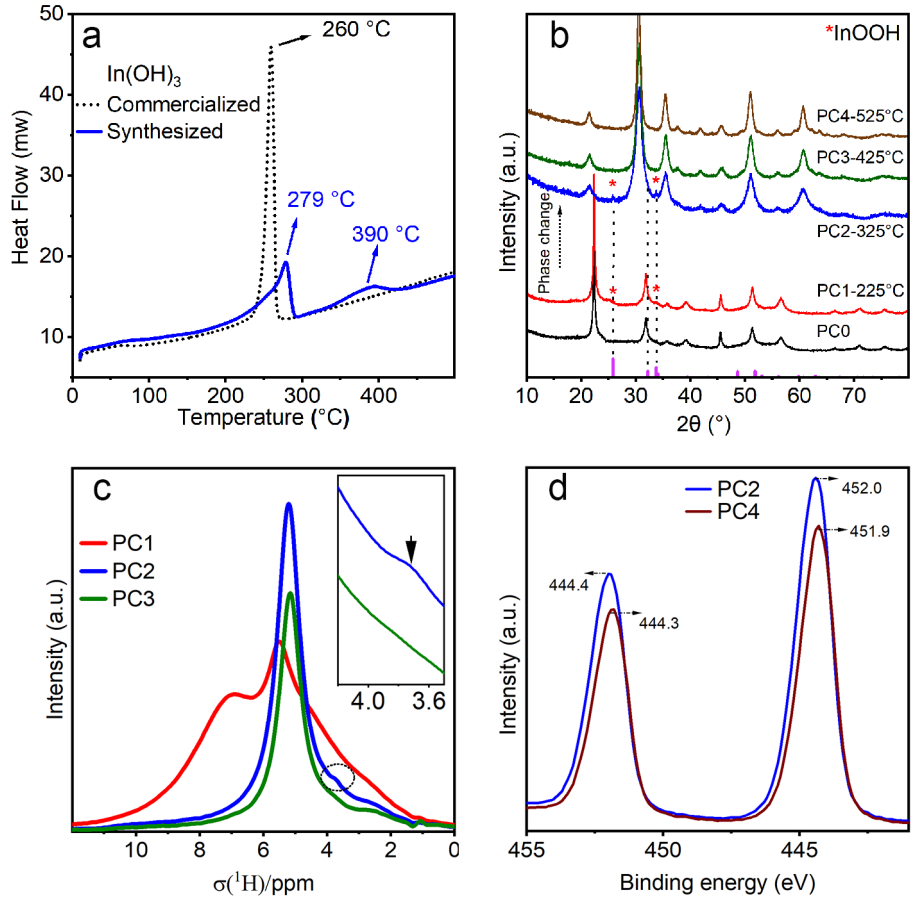

Figure 1. (a) DSC curves of as-synthesized (PC0) and commercialised $In(OH)_3$ **(b)** XRD patterns of PC0-4 samples , **(c)** a solid-state ^1H NMR spectra of PC1-3 samples; **(d)** In3d Deconvoluted peaks for PC2 and PC4.

This demonstrates that unlike commercialised $In(OH)_3$, as-synthesized $In(OH)_3$ experiences a different scenario when it is heat-treated and decomposed into In_2O_3 where the minor intermediate InOOH presents and form the InOOH/$In(OH)_3$ and InOOH/In_2O_3 heterojunction, respectively in PC1 and PC2. Note that the diffraction peak intensity of intermediate InOOH phase is relatively weak, the solid-state ^1H nuclear magnetic resonance (SS-^1H-NMR) spectroscopy of PC1-3 samples is hence collected to identify different chemical environments

of hydrogen (**Figure 1c**) and further confirm the existence of InOOH. It is found that the PC3, only consisting of In_2O_3, shows a peak at ~5 ppm, associated to adsorbed water molecules. This peak is also observed in PC1 and 2. In addition, a weak shoulder at ~3.6ppm is observable in PC2. Considering that PC2 contains both InOOH and In_2O_3, it can be assigned to the hydrogen in InOOH. In PC1, the peak at ~7.0ppm arises from $In(OH)_3$ [31]. Except for this, an asymmetric peak profile obviously appeared on the left side of peak at ~5.0 ppm indicates an additional intensity that is probably attributed to hydrogen in InOOH since InOOH indeed co-exists with $In(OH)_3$ in PC1 [32]. This further confirms the coexistence of InOOH with either $In(OH)_3$ in PC1 or In_2O_3 in PC2. **Figure 2d** illustrates deconvoluted peaks of In 3d XPS for PC2 and PC4. A shift to lower binding energy from PC2 to pure PC4 can be ascribed to the removal of the InOOH component [33]. Such a shift usually occurs for metal hydroxides compared to their equivalent oxidation state metal oxide [34]. Note that although as-synthesized $In(OH)_3$ experiences the chemical decomposition and associated structural evolution, all PC0-4 show the same sea anemone-like morphology as shown in e.g. **Figure S5b** (**Figure S5**). Such a morphology retains unchanged, without any observable structural collapse although the size slightly changes as they have been completely or partially changed to different materials. This implies that InOOH, $In(OH)_3$ and In_2O_3 in PC1 and PC2 are potentially intergrown one another, i.e. two materials are chemically assembled and interpenetrated. This has been clearly demonstrated e.g. through a typical high-resolution TEM (HRTEM) image of PC2 (**Figures 2a&b)**: different atomic image regions can be found with the d-spacing of 0.292 nm and 0.344 nm, which are attributed to the (222) planes of cubic In_2O_3 and (110) planes of orthorhombic InOOH. To carry out the Fast Fourier transform (FFT), corresponding diffraction patterns can be deduced, which are consistent with the XRD patterns of InOOH and In_2O_3. Most importantly, such two regions are closely interconnected with only a few atomic-scale boundary (pointed by blue arrows in **Figure 2a)**. Also, HRTEM in **Figure 2b** illustrates vividly

the atomic-scale interfaces in higher resolution between InOOH and In_2O_3 corresponding by the illustration of contact area at the interface. This clearly demonstrates the nature of intergrowth between InOOH and In_2O_3, implying the formation of intergrown heterojunction in PC2. More HRTEM images of orthorhombic InOOH particles taken from different areas are given in **Figure S6**. The special feature of such intergrown heterojunction is that structurally, the interfacial region is narrowed down to a few atomic-scales and hence can naturally avoid any potential band-bending and subsequently mismatching of their band structures, caused by chemical and structural variation in this region, eventually facilitating or accelerating the interfacial charge carrier transferring (**Figure 2c**).

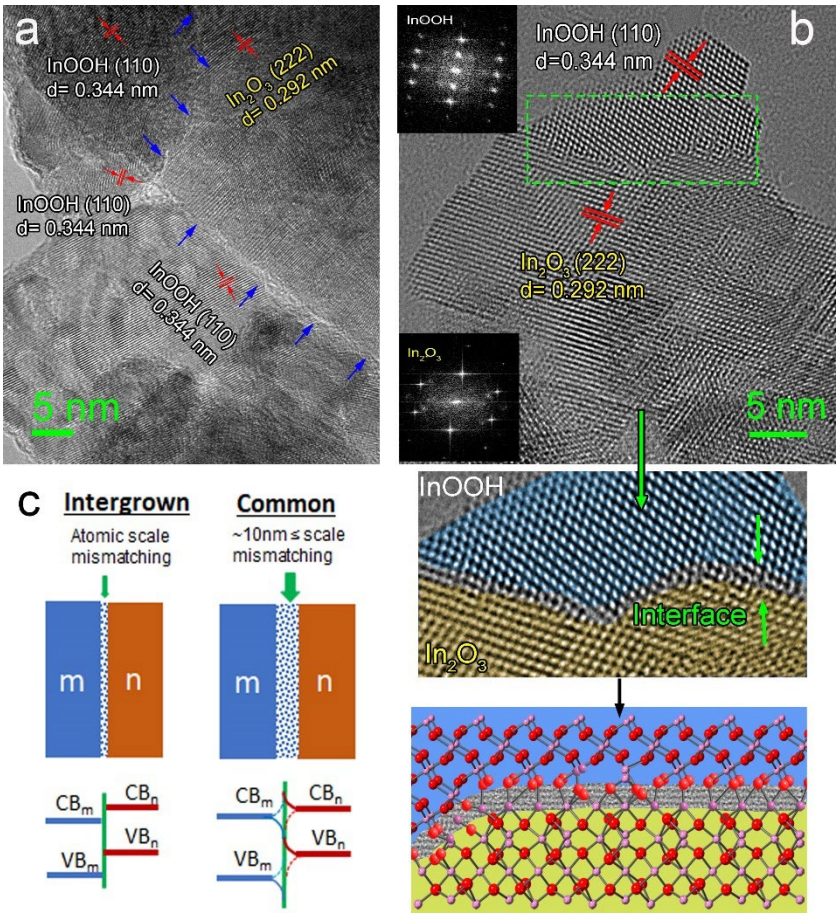

Figure 2. (a&b) HRTEM images collected from PC2 and their FFT results clearly indicate the nature of interfacial connection between In_2O_3 and InOOH (blue arrows), and (**c**) a schematic drawing to show the intergrown heterojunction may be more interfacial controllable in comparison with the common heterojunction with a broad interfacial region. The band-bending may happen in the relatively large-scale interfacial region of heterojunction caused by chemical inhomogeneity and/or structural variation.

3.2. Degradation of PFOAs

Figure 3a presents the principle of degradation of PFOAs using In_2O_3 photocatalysts as an example. As reported previously [35, 36], the terminal carboxylate group of PFOA molecule tightly coordinates to the In_2O_3 surface in a bidentate or bridging configuration, which is beneficial for PFOA to be directly decomposed by photogenerated holes of In_2O_3 under UV irradiation. PC0-4 samples, serving as photocatalysts, were used for decomposing PFOAs under an UV (254 nm) light irradiation. **Figure 3a** shows their PFOA decomposition performance under the same condition. The degradation rate shows the trend like PC2 (85.5%) > PC1 (54.1%) > PC3 (44%) > PC4 (32.4%) > PC0 (26.2%). This result cannot be explained in terms of their trends on surface areas: PC3 (260 m^2g^{-1}) > PC2 (241 m^2g^{-1}) > PC4 (139 m^2g^{-1}) in In_2O_3-contained samples, and PC0 (23 m^2g^{-1}) >PC1 (15 m^2g^{-1}) in $In(OH)_3$-contained samples (**Figure S7**). Notwithstanding that a high specific surface area can boost the photocatalytic performance by either presenting more active sites or better adsorption of adsorbate on the surface of photocatalyst, nonphysical factors are crucial and dominant. Nonetheless, the influence of surface area can be explained to compare the PC3 and PC4, where both only contain In_2O_3. The degradation efficiency in PC3 is higher than that in PC4 due to the high specific surface areas in PC3. Obviously, the large surface area will make contribution towards the high photocatalytic performance, but it is not predominated because the PC0 and PC1, PC3 and PC2 have similar surface areas, but PC1 and PC2 have much better catalytic performance even though their surface areas are slightly lower than that of the PC0 and PC3. This clearly demonstrate that the intergrown heterojunction structure will significantly improve the catalytic behaviours, since the photocatalytic property of heterojunction photocatalysts would potentially be affected by the change in the crystallinity, morphology, active site density and defect density [39, 40]. Meanwhile, surface area increments from PC1 to PC4 can be

assigned to the generation of mesopores during annealing processes as shown and discussed in **Figure S7**.

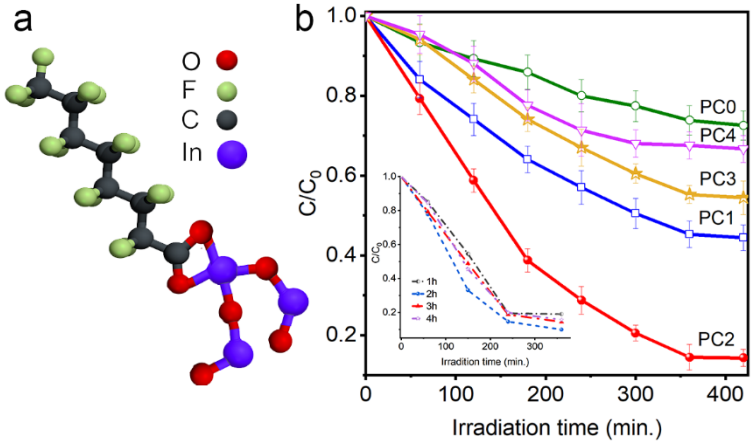

Figure 3. Photocatalytic degradation of PFOAs (a) principle where the illustration of PFOA coordination to In_2O_3 surface via bridging bidentate mode. (b) using PC0-4 (treated for 3 hours) as catalysts. The inset presents the result using the catalysts treated PC0 at 325°C for different times, where the catalysts obtained by heat-treated for 2 hours shows the best performance.

As the best catalytic performance observed when PC2 is used. The heat treatments at this temperature, *i.e.* 325°C for various times (1-4 hours) were also performed to further optimise the catalysts. As a result, over 90.1% degradation rate has already achieved for the sample treated for 2 hours (as shown in the inset, **Figure 3b**). It can then be deduced that the presence and formation of InOOH and building *intergrown* biphasic heterostructure with either $In(OH)_3$ or In_2O_3 phase is crucial to boost their photocatalytic performance. We also introduce the first-order kinetic model [37] to assess the PFOA's degradation performance. **Table S2** shows the results obtained by using PC0-4 as catalysts. The apparent reaction rate constant is 5.62×10^{-3} min^{-1} for PC2 and 3.79×10^{-3} min^{-1} for PC1. Both intergrown heterojunction catalysts show much faster reaction than that PC3 (1.78×10^{-3} min^{-1}), not to mention others. Furthermore, the reusability and stability of the photocatalyst are critical factors for the catalysts in practical applications. For this purpose, the XRD is used to monitor the change after each cycle of catalytic reaction. We run three cycles using the same PC2, and find no change in either

catalytic behaviour and their structure, which suggests that such intergrown catalysts are reasonably stable and reusable (**Figure S8**).

3.3. Spectral analysis

To obtain a deeper understanding of the enhanced photocatalytic performance observed in such an intergrown InOOH/In_2O_3 (PC2) and InOOH/$In(OH)_3$ (PC1) heterojunction photocatalysts, it is essential to investigate their optical absorption spectra. Unfortunately, $In(OH)_3$ has a very large bandgap, the absorption of PC0 and PC1 cannot be measured using our available instrument. **Figure 4a** shows optical absorbance of PC2-4 samples where the pure InOOH sample has also been added for comparison. It is found that the PC2, i.e. intergrown InOOH/In_2O_3 heterojunction photocatalyst, exhibits a remarkable extension of light absorption into the visible region compared to pure InOOH or In_2O_3, even in the case of PC3 whose morphology and surface area are close to that of PC2. This well experimentally demonstrates such an intergrown heterojunction has significantly change the optical absorption capability. Such absorption extension can promote light harvesting in the visible region [38]. In addition, using the spectral data of **Figure 4a** and the transformed Kubelka−Munk function [39], the optical bandgap of pure InOOH and PC2-4 is determined to be 3.70, 3.13, 3.07, and 3.02 eV, respectively. The absorption edge of PC2 photocatalyst is slightly higher than PC4 due to the presence of InOOH with a wider band gap of ca. 3.7 eV [19]. Their valence band (VB) edge position can deduced from experimental X-ray photoelectron spectroscopy (XPS) as shown in **Figure 4b**. For instance, the VB energy levels are 2.65 and 2.32 eV for InOOH/In_2O_3 and In_2O_3, respectively. By comparison the VB values of PC4 obtained from experiment and calculation, there is a good agreement with a reasonable difference (0.06 eV, ca. 2.5%), suggesting this approach is feasible and reliable. The CB energy levels can be determined based on the bandgap and its VB position. These provide the values for constructing the band structure (e.g. **Figure 5b** below) of heterojunction catalysts for further discussion. **Figure 4c**

is the PL spectra of PC2, PC4 and InOOH excited by a 405 nm laser. All these present broad emission peaks with the wavelength across entire visible-near infrared range. These results, in conjunction with the absorption spectra presented in **Figure 4a**, suggest the defect energy band exists within the forbidden gap of InOOH and PC4 as well as PC0. This is consistent with the previous reports [20]. Interestingly two peaks are observed in PC2. The strongest peak, located at ~550nm and in between the emission peaks of InOOH and In_2O_3, can be assigned to the combination of emissions from both InOOH and In_2O_3. An additional emission peak shoulder at over 600 nm in PC2, however cannot be explained by such a combination.

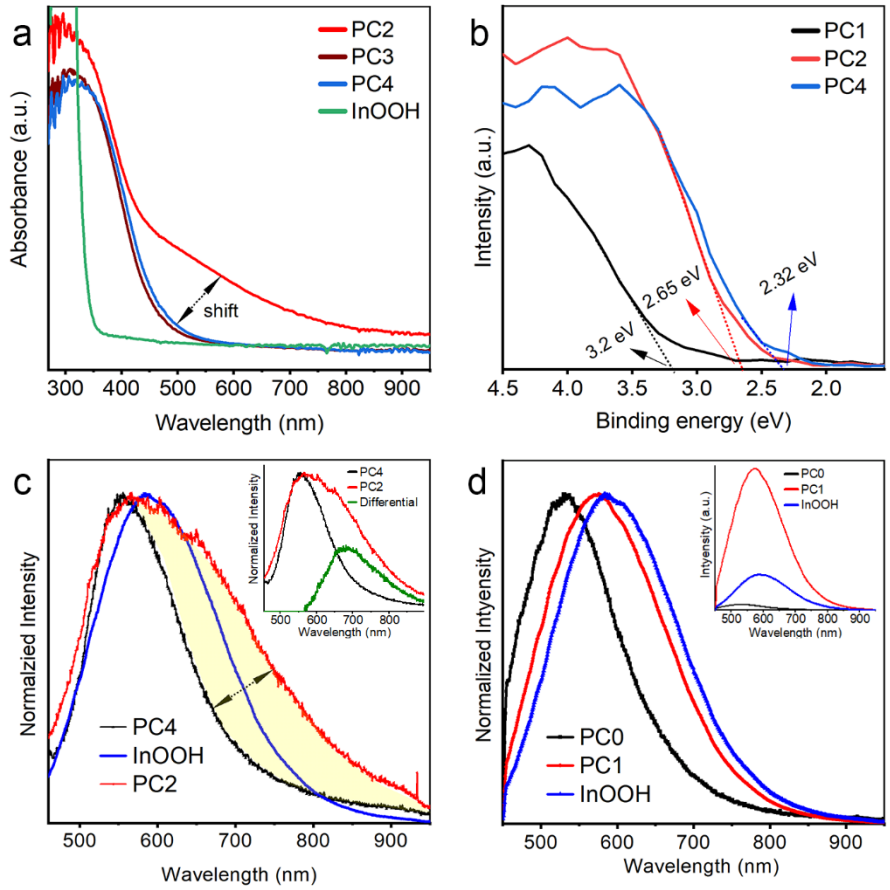

Figure 4. (a) Optical absorption of PC2-4 and InOOH, **(b)** Partial XPS spectra that show the valance band edge positions of PC1-3, and **(c)** steady PL spectra of PC2, InOOH and PC4 excited under 405nm light, **(d)** steady PL spectra of PC0, InOOH and PC1 excited under 405nm light.

Such an emission with a big tail in lower energy side (i.e. near infrared region) suggests potential interaction may occur between InOOH and In_2O_3, associated with the cross-band

excitation, emission and recombination, i.e. charge carrier transferring at the interfacial region of InOOH and In_2O_3 in such an intergrown InOOH/In_2O_3 heterojunction photocatalyst. By contrast, From **Figure 4d**, we cannot see such a type of interaction between $In(OH)_3$ and InOOH, implying less interaction between these two.

3.4 Interfacial charge carrier transferring occurred in intergrown InOOH/In_2O_3

To further investigate possible charge carrier transferring within intra-band, we investigate its photogenerated carrier dynamic processes using the steady photoluminescent (PL) and time-resolved PL (TRPL) techniques that allow quantitative comparison of PL intensity. The inset in **Figure 4c** compares the PL intensities of PC2, InOOH, and PC4 with excitation of 405 nm at identical conditions. The PL intensity of InOOH is much higher than those of PC4. In PC2, it is therefore expected that its PL intensity would increase but should not be such significant with a small amount of InOOH as indicated from the XRD, if the enhanced PL is only from the InOOH itself. This also suggests an additional effect may presents in PC2 that would potentially enhance its PL intensity. The TRPL was further investigated to get corresponding PL delay curves presented in **Figure 5a**. Each PL decay curve can be well fitted by three-exponential decay function in order to obtain quantitative analysis of PL decay processes and the fitting parameters are summarized in **Table 1**.

Table 1. Kinetic parameters of decays observed for understudy Samples.

Parameters	*InOOH/In_2O_3 (ns)*	*InOOH (ns)*
A_1	2914.35	2117.40
τ_1	0.40	0.51
A_2	964.83	1750.16
τ_2	1.68	1.95
A_3	84.58	265.67
τ_3	7.11	6.23
τ_{eff}	0.857	1.535

The intergrown InOOH/In_2O_3 exhibits significantly shorter effective lifetime, 0.857 ns, compared to that of InOOH of 1.535 ns. (**SI:** $\tau_{eff} = \frac{A_1\tau_1+A_2\tau_2}{A_1+A_2}$) [40]. This can be explained

based on the energy alignment of InOOH/In_2O_3 schematically shown in **Figure 5b** upon excitation by the photons of 405 nm, the electrons are photogenerated to both the excited states (metastable) of InOOH and the VB of In_2O_3. The possible relaxation pathways for the excited electrons include: (1) the electrons recombine with the holes in InOOH and emit photons; corresponding to the PL spectrum of InOOH. (2) the electrons recombine with the holes in In_2O_3 and emit photons; corresponding to the PL spectrum of In_2O_3. (3) the holes can transfer from the VB of InOOH into the VB of In_2O_3. This pathway acts as a competitive channel for InOOH recombination and will result in lowering PL intensity (quenching) together with the decreased PL lifetime in Intergrown InOOH/In_2O_3 photocatalysts. (4) the electrons in InOOH (metastable states) recombine with the holes in the valance band of In_2O_3 (2.26 eV). This transition occurs only when they have sufficient interaction in the heterostructure and results in the additional emission beyond the pure InOOH and In_2O_3 in the red side, as shown in **Figures 4c** and **5b,** which is consistent with their optical absorption with a long tail of absorption in near infrared region.

The hole transfer rate InOOH/In_2O_3 in Intergrown InOOH/In_2O_3 can be estimated using the measured PL lifetimes by [48]

$$R_{transfer} = \frac{1}{\tau_{InOOH-In2O3}} = \frac{1}{\tau_{InOOH}} + \frac{1}{\tau_{transfer}}$$

$$R_{transfer} = \left(\frac{1}{0.857} - \frac{1}{1.535}\right) \times 10^9 = 0.516 \times 10^9$$

Where the τ are lifetimes and $R = 1/\tau$ is the transfer rate. Such short transferring time is well explained the interfacial charge carrier transferring that interact between InOOH and In_2O_3 band structure. In this case the extra holes in the valance band of In_2O_3 result in significantly increased probability for redox, and eventually achieve the enhanced photocatalytic performance (**Figure 3b**). Moreover, maintaining electrical neutrality in the catalyst is prerequisite for sustainable photocatalysis. It should note that the redox may be insufficiently fast to relax all excited holes back to the valence band.

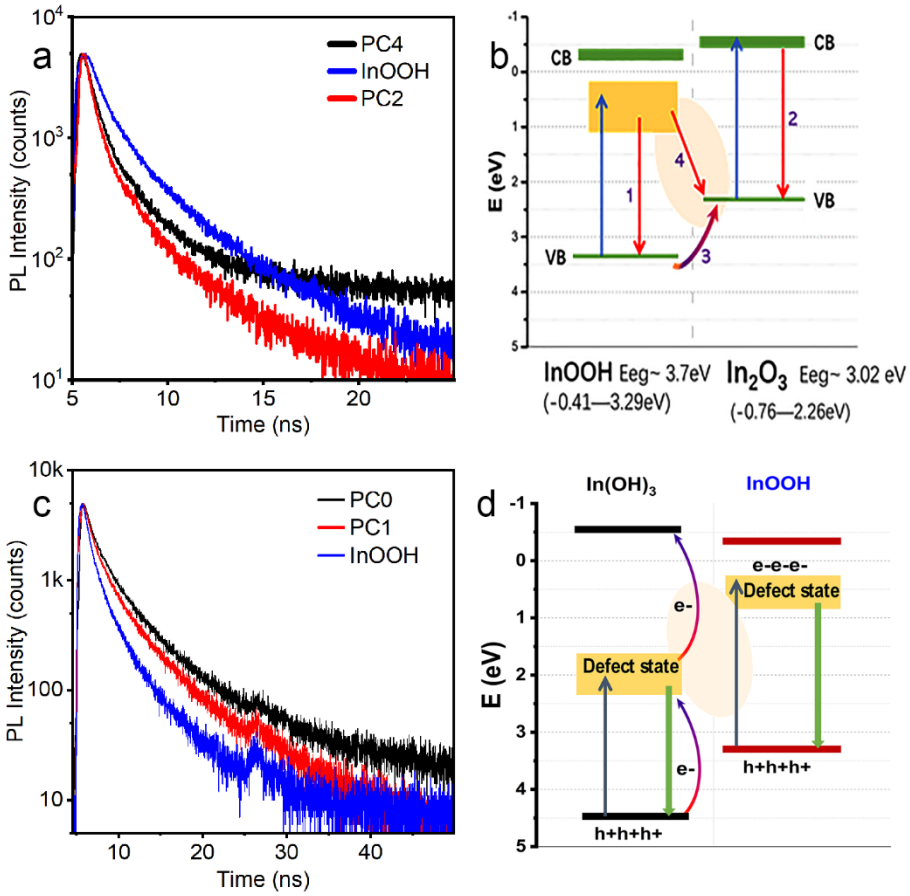

Figure 5. (a) Nanosecond full range TRPL with normalized optical density (OD) for InOOH/In_2O_3 (PC2) and their comparisons; **(b)** Possible charge transfer illustration in InOOH/In_2O_3 heterojunction photocatalysts; **(c)** FTRPL of $In(OH)_3$, InOOH /$In(OH)_3$ (PC1) and InOOH **(d)** Possible charge transfer illustration in intergrown assembly of PC1 heterojunction photocatalysts. Excitation:405 nm.

The recombination the electrons in the conduction band of InOOH and holes in the valence band of In_2O_3 can be an additional channel. This recombination result in the observed NIR band in the intergrown InOOH/In_2O_3 photocatalysts.

3.5 None interfacial charge carrier transferring in Intergrown InOOH/$In(OH)_3$

According to the results presented in **Figure 4d**, the interaction between $In(OH)_3$ and InOOH in PC1 heterojunction is not obvious. This is because the PL spectrum of PC1 is approximately the weighted average of the PL spectra of $In(OH)_3$ and InOOH, with no discernible additional near inferred intensity, which strongly suggests the interaction between $In(OH)_3$ and InOOH is negligible. The PL decay curves (**Figure 5c**) show that PL decay of PC1 is roughly the average of $In(OH)_3$ and InOOH, consistent with negligible charge transfer occur between

$In(OH)_3$ and InOOH, in turn indicating negligible interaction between the two components. The energy alignment of PC1 is shown schematically in **Figure 5d.** In a nutshell, the two components in intergrown PC1 act merely as a simple mixture. It might be expected that the performance of PC1 is approximately the average of individual $In(OH)_3$ and InOOH. However, considering possible interface passivation effects for suppression of the nonradiative channel in compound of PC1, its performance can be better than $In(OH)_3$ and InOOH. The increased PL efficiency can consistently support this conclusion.

4. Conclusion

In summary, we have reported how to grow intergrown heterojunction catalysts starting from as-synthesized $In(OH)_3$ as a precursor, where intermediate InOOH appears, leading to *intergrown* biphasic InOOH/In_2O_3 (PC2) and InOOH/$In(OH)_3$ (PC1). PC2 presents outstanding photocatalytic performances, which is much better than the PC1. This is because the intergrown PC2 heterojunction not only provides well-matched band structure but also enables the interfacial charge transferring to occur in PC2 but not in PC1. The enhancement of PC1 in photocatalytic effect may only benefit from the resultant active sites, interfacial passivation effect etc that normally occurs in common heterojunction catalysts. The optimised intergrown InOOH/In_2O_3 heterojunction catalysts show the best degradation performance on PFOAs, providing a new insight on the design and development of new heterojunction catalysts whilst paving the way to utilise this new catalyst for highly efficient remediation of the PFOA-contaminated water with a promising potential via green and renewable solar energy.

Acknowledgements

FN, TL, TF and YL acknowledge the support of the Australian Research Council through Discovery Projects (DP190100295, DP200100159) and Laureate Fellow (FL210100017) funding scheme.

CRediT authorship contribution statement

FN contributed to the initial idea, conceptualization, experimental design, result analysis, investigation, and draft-writing, XW conducted special steady PL and TRPL and draft this part of the manuscript. QS and TL provide mentoring in hydrothermal reaction and XRD analysis, ZZ, FK and ZL collect various HRTEM images. HO, EAA and GO did routine PL and ^{1}H NMR, BL and AT did surface area characterisation, SN and TF did theoretical analysis, TF and YL coordinate the project, assist in data analysis, and supervise the research. All the authors made their contribution to data analysis and draft-writing.

Conflict of interest

The authors declare no conflict of interest.

Reference

[1] F. Nekouei, S. Nekouei, M. Pouzesh, Y. Liu, Porous-CdS/Cu2O/graphitic-C3N4 dual p-n junctions as highly efficient photo/catalysts for degrading ciprofloxacin and generating hydrogen using solar energy, Chemical Engineering Journal 385 (2020) 123710. https://doi.org/https://doi.org/10.1016/j.cej.2019.123710.

[2] W. Yu, T. Zhang, Z. Zhao, Garland-like intercalated carbon nitride prepared by an oxalic acid-mediated assembly strategy for highly-efficient visible-light-driven photoredox catalysis, Applied Catalysis B: Environmental 278 (2020) 119342. https://doi.org/https://doi.org/10.1016/j.apcatb.2020.119342.

[3] S. Gao, X. Wang, C. Song, S. Zhou, F. Yang, Y. Kong, Engineering carbon-defects on ultrathin g-C3N4 allows one-pot output and dramatically boosts photoredox catalytic activity, Applied Catalysis B: Environmental 295 (2021) 120272. https://doi.org/https://doi.org/10.1016/j.apcatb.2021.120272.

[4] J. Kosco, M. Bidwell, H. Cha, T. Martin, C.T. Howells, M. Sachs, D.H. Anjum, S.G. Lopez, L. Zou, A. Wadsworth, Enhanced photocatalytic hydrogen evolution from organic semiconductor heterojunction nanoparticles, Nature Materials 19(5) (2020) 559-565.

[5] Z. Miao, Q. Wang, Y. Zhang, L. Meng, X. Wang, In situ construction of S-scheme AgBr/BiOBr heterojunction with surface oxygen vacancy for boosting photocatalytic CO2 reduction with H2O, Applied Catalysis B: Environmental 301 (2022) 120802. https://doi.org/https://doi.org/10.1016/j.apcatb.2021.120802.

[6] Y. Zhou, C. Zhang, D. Huang, W. Wang, Y. Zhai, Q. Liang, Y. Yang, S. Tian, H. Luo, D. Qin, Structure defined 2D Mo2C/2Dg-C3N4 Van der Waals heterojunction: Oriented charge flow in-plane and separation within the interface to collectively promote photocatalytic degradation of pharmaceutical and personal care products, Applied Catalysis B: Environmental 301 (2022) 120749. https://doi.org/https://doi.org/10.1016/j.apcatb.2021.120749.

[7] O. Voznyy, B.R. Sutherland, A.H. Ip, D. Zhitomirsky, E.H. Sargent, Engineering charge transport by heterostructuring solution-processed semiconductors, Nature Reviews Materials 2(6) (2017) 1-10.

[8] J. Low, J. Yu, M. Jaroniec, S. Wageh, A.A. Al-Ghamdi, Heterojunction photocatalysts, Advanced materials 29(20) (2017) 1601694.

[9] Y. Dong, Y. Su, Y. Hu, H. Li, W. Xie, Ag2S-CdS p-n Nanojunction-Enhanced Photocatalytic Oxidation of Alcohols to Aldehydes, Small 16(47) (2020) 2001529.
[10] S. Ni, H. Qu, Z. Xu, X. Zhu, H. Xing, L. Wang, J. Yu, H. Liu, C. Chen, L. Yang, Interfacial engineering of the NiSe2/FeSe2 p-p heterojunction for promoting oxygen evolution reaction and electrocatalytic urea oxidation, Applied Catalysis B: Environmental 299 (2021) 120638. https://doi.org/https://doi.org/10.1016/j.apcatb.2021.120638.
[11] H. Xu, Y. Wang, X. Dong, N. Zheng, H. Ma, X. Zhang, Fabrication of In2O3/In2S3 microsphere heterostructures for efficient and stable photocatalytic nitrogen fixation, Applied Catalysis B: Environmental 257 (2019) 117932. https://doi.org/https://doi.org/10.1016/j.apcatb.2019.117932.
[12] Y.-X. Pan, Y. You, S. Xin, Y. Li, G. Fu, Z. Cui, Y.-L. Men, F.-F. Cao, S.-H. Yu, J.B. Goodenough, Photocatalytic CO2 Reduction by Carbon-Coated Indium-Oxide Nanobelts, Journal of the American Chemical Society 139(11) (2017) 4123-4129. https://doi.org/10.1021/jacs.7b00266.
[13] L.B. Hoch, L. He, Q. Qiao, K. Liao, L.M. Reyes, Y. Zhu, G.A. Ozin, Effect of precursor selection on the photocatalytic performance of indium oxide nanomaterials for gas-phase CO2 reduction, Chemistry of Materials 28(12) (2016) 4160-4168.
[14] L. He, T.E. Wood, B. Wu, Y. Dong, L.B. Hoch, L.M. Reyes, D. Wang, C. Kübel, C. Qian, J. Jia, K. Liao, P.G. O'Brien, A. Sandhel, J.Y.Y. Loh, P. Szymanski, N.P. Kherani, T.C. Sum, C.A. Mims, G.A. Ozin, Spatial Separation of Charge Carriers in In2O3–x(OH)y Nanocrystal Superstructures for Enhanced Gas-Phase Photocatalytic Activity, ACS Nano 10(5) (2016) 5578-5586. https://doi.org/10.1021/acsnano.6b02346.
[15] O. Zandi, A. Agrawal, A.B. Shearer, L.C. Reimnitz, C.J. Dahlman, C.M. Staller, D.J. Milliron, Impacts of surface depletion on the plasmonic properties of doped semiconductor nanocrystals, Nature Materials 17(8) (2018) 710-717. https://doi.org/10.1038/s41563-018-0130-5.
[16] M.S. Frei, C. Mondelli, A. Cesarini, F. Krumeich, R. Hauert, J.A. Stewart, D. Curulla Ferré, J. Pérez-Ramírez, Role of Zirconia in Indium Oxide-Catalyzed CO2 Hydrogenation to Methanol, ACS Catalysis 10(2) (2020) 1133-1145. https://doi.org/10.1021/acscatal.9b03305.
[17] Y. Qi, L. Song, S. Ouyang, X. Liang, S. Ning, Q. Zhang, J. Ye, Photoinduced Defect Engineering: Enhanced Photothermal Catalytic Performance of 2D Black In2O3− x Nanosheets with Bifunctional Oxygen Vacancies, Advanced Materials 32(6) (2020) 1903915.
[18] F. Lei, Y. Sun, K. Liu, S. Gao, L. Liang, B. Pan, Y. Xie, Oxygen Vacancies Confined in Ultrathin Indium Oxide Porous Sheets for Promoted Visible-Light Water Splitting, Journal of the American Chemical Society 136(19) (2014) 6826-6829. https://doi.org/10.1021/ja501866r.
[19] J. Li, K. Li, B. Lei, M. Ran, Y. Sun, Y. Zhang, K.-H. Kim, F. Dong, High-efficiency photocatalytic decomposition of toluene over defective InOOH: Promotive role of oxygen vacancies in ring opening process, Chemical Engineering Journal (2020) 127389.
[20] Y. Zhuang, J. Luan, Improved photocatalytic property of peony-like InOOH for degrading norfloxacin, Chemical Engineering Journal 382 (2020) 122770.
[21] Z. Yi, J. Ye, N. Kikugawa, T. Kako, S. Ouyang, H. Stuart-Williams, H. Yang, J. Cao, W. Luo, Z. Li, Y. Liu, R.L. Withers, An orthophosphate semiconductor with photooxidation properties under visible-light irradiation, Nature Materials 9(7) (2010) 559-564. https://doi.org/10.1038/nmat2780.
[22] X. Zhang, Y. Lin, D. He, J. Zhang, Z. Fan, T. Xie, Interface junction at anatase/rutile in mixed-phase TiO2: Formation and photo-generated charge carriers properties, Chemical Physics Letters 504(1) (2011) 71-75. https://doi.org/https://doi.org/10.1016/j.cplett.2011.01.060.
[23] G. Merle, D. Bassett, J. Finch, G. Demopoulos, J. Barralet, Self-assembled photoactive heterojunction phase gradient, Journal of Materials Chemistry A 2(23) (2014) 8868-8874.
[24] F.T.F. O'Mahony, T. Lutz, N. Guijarro, R. Gómez, S.A. Haque, Electron and hole transfer at metal oxide/Sb2S3/spiro-OMeTAD heterojunctions, Energy & Environmental Science 5(12) (2012) 9760-9764. https://doi.org/10.1039/C2EE23037B.
[25] C. Li, S. Ma, P. Wei, W. Zhu, X. Nie, X. Sang, Z. Sun, Q. Zhang, W. Zhao, Magnetism-induced huge enhancement of the room-temperature thermoelectric and cooling performance of p-type BiSbTe alloys, Energy & Environmental Science 13(2) (2020) 535-544. https://doi.org/10.1039/C9EE03446C.

[26] J. Wang, C. Cao, Y. Zhang, Y. Zhang, L. Zhu, Underneath mechanisms into the super effective degradation of PFOA by BiOF nanosheets with tunable oxygen vacancies on exposed (101) facets, Applied Catalysis B: Environmental 286 (2021) 119911. https://doi.org/https://doi.org/10.1016/j.apcatb.2021.119911.
[27] H. Tang, W. Zhang, Y. Meng, S. Xia, A direct Z-scheme heterojunction with boosted transportation of photogenerated charge carriers for highly efficient photodegradation of PFOA: Reaction kinetics and mechanism, Applied Catalysis B: Environmental 285 (2021) 119851. https://doi.org/https://doi.org/10.1016/j.apcatb.2020.119851.
[28] C.-Y. Li, S.-x. Liu, Template-free synthesis of morphology-and size-controlled nano indium hydroxide, International Journal of Minerals, Metallurgy, and Materials 19(12) (2012) 1154-1161.
[29] J. Liu, G. Chen, Y. Yu, Y. Wu, M. Zhou, H. Zhang, C. Lv, Y. Zheng, F. He, Controllable synthesis of In 2 O 3 octodecahedra exposing {110} facets with enhanced gas sensing performance, RSC Advances 5(55) (2015) 44306-44312.
[30] L. Schlicker, M.F. Bekheet, A. Gurlo, Scaled-up solvothermal synthesis of nanosized metastable indium oxyhydroxide (InOOH) and corundum-type rhombohedral indium oxide (rh-In2O3), Zeitschrift für Kristallographie-Crystalline Materials 232(1-3) (2017) 129-140.
[31] X. Xue, M. Kanzaki, High-pressure δ-Al (OH) 3 and δ-AlOOH phases and isostructural hydroxides/oxyhydroxides: New structural insights from high-resolution 1H and 27Al NMR, The Journal of Physical Chemistry B 111(46) (2007) 13156-13166.
[32] J. Chen, M.A. Hope, Z. Lin, M. Wang, T. Liu, D.M. Halat, Y. Wen, T. Chen, X. Ke, P.C. Magusin, Interactions of Oxide Surfaces with Water Revealed with Solid-State NMR Spectroscopy, Journal of the American Chemical Society (2020).
[33] Z.M. Detweiler, S.M. Wulfsberg, M.G. Frith, A.B. Bocarsly, S.L. Bernasek, The oxidation and surface speciation of indium and indium oxides exposed to atmospheric oxidants, Surface Science 648 (2016) 188-195.
[34] C. Donley, D. Dunphy, D. Paine, C. Carter, K. Nebesny, P. Lee, D. Alloway, N.R. Armstrong, Characterization of Indium− Tin oxide interfaces using X-ray photoelectron spectroscopy and redox processes of a chemisorbed probe molecule: effect of surface pretreatment conditions, Langmuir 18(2) (2002) 450-457.
[35] X. Li, P. Zhang, L. Jin, T. Shao, Z. Li, J. Cao, Efficient Photocatalytic Decomposition of Perfluorooctanoic Acid by Indium Oxide and Its Mechanism, Environmental Science & Technology 46(10) (2012) 5528-5534. https://doi.org/10.1021/es204279u.
[36] Z. Li, P. Zhang, T. Shao, J. Wang, L. Jin, X. Li, Different nanostructured In2O3 for photocatalytic decomposition of perfluorooctanoic acid (PFOA), Journal of Hazardous Materials 260 (2013) 40-46. https://doi.org/https://doi.org/10.1016/j.jhazmat.2013.04.042.
[37] K.A. Connors, Chemical kinetics: the study of reaction rates in solution, Wiley-VCH Verlag GmbH1990.
[38] X.Z. Li, F.B. Li, Study of Au/Au3+-TiO2 Photocatalysts toward Visible Photooxidation for Water and Wastewater Treatment, Environmental Science & Technology 35(11) (2001) 2381-2387. https://doi.org/10.1021/es001752w.
[39] P. Kubelka, Ein Beitrag zur Optik der Farbanstriche (Contribution to the optic of paint), Zeitschrift fur technische Physik 12 (1931) 593-601.
[40] X. Wen, Y. Feng, S. Huang, F. Huang, Y.-B. Cheng, M. Green, A. Ho-Baillie, Defect trapping states and charge carrier recombination in organic–inorganic halide perovskites, Journal of Materials Chemistry C 4(4) (2016) 793-800.